

# Upside-down fluxes Down Under: CO<sub>2</sub> net sink in winter and net source in summer in a temperate evergreen broadleaf forest

Alexandre A. Renchon<sup>1</sup>, Anne Griebel<sup>1</sup>, Daniel Metzen<sup>1</sup>, Christopher A. Williams<sup>2</sup>, Belinda Medlyn<sup>1</sup>, Remko A. Duursma<sup>1</sup>, Craig VM Barton<sup>1</sup>, Chelsea Maier<sup>1</sup>, Matthias M. Boer<sup>1</sup>, Peter Isaac<sup>3</sup>, David Tissue<sup>1</sup>, Victor Resco de Dios<sup>4</sup>, Elise Pendall<sup>1</sup>

<sup>1</sup>Hawkesbury Institute for the Environment, Western Sydney University, Penrith, NSW, Australia.

<sup>2</sup>Clark University, Graduate School of Geography, Worcester, Massachusetts 01610, USA.

<sup>3</sup>CSIRO Oceans & Atmosphere Flagship, Yarralumla, ACT, 2600, Australia.

<sup>4</sup>Department of Crop and Forest Sciences and Agrotecnio Center, University of Lleida, E-25198 Lleida, Spain.

## Abstract

Predicting the seasonal dynamics of ecosystem carbon fluxes is challenging in broadleaved evergreen forests because of their moderate climates and subtle changes in canopy phenology. We assessed the climatic and biotic drivers of the seasonality of net ecosystem-atmosphere CO<sub>2</sub> exchange (NEE) of a eucalyptus-dominated forest near Sydney, Australia, using the eddy covariance method. The climate is characterized by a mean annual precipitation of 800 mm and a mean annual temperature of 18 °C, hot summers and mild winters, with highly variable precipitation. In the four-year study, the ecosystem was a sink each year (-225 g C m<sup>-2</sup> y<sup>-1</sup> on average, with a standard deviation of 108 g C m<sup>-2</sup> y<sup>-1</sup>); inter-annual variations were not related to meteorological conditions. Daily net C uptake was always detected during the cooler, drier winter months (June through August), while net C loss occurred during the warmer, wetter summer months (December through February). Gross primary productivity (GPP) seasonality was low, despite longer days with higher light intensity in summer, because vapour pressure deficit (D) and air temperature (T<sub>a</sub>) restricted surface conductance during summer while winter temperatures were still high enough to support photosynthesis. Maximum GPP during ideal environmental conditions was significantly correlated with remotely sensed enhanced vegetation index (EVI, r<sup>2</sup> = 0.46) and with canopy leaf area index (LAI, r<sup>2</sup> = 0.24), which increased rapidly after mid-summer rainfall events. Ecosystem respiration (ER) was highest during summer in wet soils and lowest during winter months. ER had larger seasonal amplitude compared to GPP, and therefore drove the seasonal variation of NEE. Because summer carbon uptake may become increasingly limited by atmospheric demand and high temperature, and ecosystem respiration could be enhanced by rising temperature, our results suggest the potential for large-scale seasonal shifts in NEE in sclerophyll vegetation under climate change.

*Keywords:* net ecosystem exchange, seasonal variability, atmospheric demand, canopy phenology

## 1. Introduction

Forests and semi-arid biomes are responsible for the majority of global carbon storage by terrestrial ecosystems (Dixon et al. 1994; Pan et al. 2011; Poulter et al. 2014; Schimel et al. 2001). Photosynthesis and respiration by these biomes strongly influence the seasonal cycle of atmospheric CO<sub>2</sub> (Baldocchi et al. 2016; Keeling et al. 2001). Continuous measurements of land-atmosphere exchanges of carbon, energy and water provide insights into the seasonality of forest ecosystem processes, which are driven by the interactions of climate, plant physiology and forest composition and structure (Xia et al. 2015). Net ecosystem exchange (NEE) seasonality is relatively well understood in cool-temperate ecosystems; deciduous trees can only photosynthesize when they have leaves and NEE dynamics are thus principally influenced by the phenology of canopy processes. NEE of deciduous forests thus has a more pronounced seasonality than that of evergreen conifer forests at similar latitudes (Novick et al. 2015). For high-latitude evergreen conifer forests, NEE seasonality is strongly limited by cold temperature limitation of photosynthesis (Kolari et al. 2007) and respiration. In contrast, seasonality of NEE in evergreen broadleaf forests, typically occurring in warm-temperate and tropical regions, is much less well understood (Restrepo-Coupe et al. 2017; Wu et al. 2016).

The seasonality of gross primary productivity (GPP) in evergreen broadleaf forests may be driven by climate (e.g. dry/wet seasons) and/or by canopy dynamics (Wu et al. 2016). In tropical evergreen forests, air temperature and day length are similar seasonally, but precipitation seasonality can be strong, with higher radiation and temperature (1 or 2 °C higher) in the dry season (Trenberth 1983; Windsor 1990). Counter-intuitively, GPP can be higher during the dry season, as cloud cover may limit productivity in the wet season (Graham et al. 2003; Hutrya et al. 2007; Saleska et al. 2003). Canopy dynamics can be an important determinant of GPP seasonality in evergreen broadleaf forests; although leaves are present in the canopy year-round in evergreen canopies, LAI may show considerable temporal variability seasonally as new leaves are produced and old leaves die, especially during leaf flush and senescence periods (Duursma et al. 2016; Wu et al. 2016). The leaf light use efficiency and water use efficiency may both vary as leaves age: young leaves and old leaves are less efficient than mature leaves, reflecting changes in photosynthetic capacity (Wilson et al. 2001; Wu et al. 2016). The timing of leaf flush and senescence can depend on the environment and on species; environmental stress, such as drought, can induce the process of senescence (Lim et al. 2007; Munné-Bosch and Alegre 2004).

In temperate evergreen broadleaved forests, such as eucalypt-dominated sclerophyll vegetation in Australia, precipitation can be seasonal or aseasonal; furthermore, day length and temperature vary significantly between winter and summer. GPP can be limited by frost during winter and by drought during summer. Atmospheric demand indicated by high vapor pressure deficit (D) and soil drought have different impacts on GPP, but they can interact to impact surface conductance (G<sub>s</sub>) (Medlyn et al. 2011; Novick et al. 2016). In Australia's temperate eucalypt forests, canopy rejuvenation takes place in summer and is linked to heavy rainfall events (Duursma et al. 2016). However, since leaf flushing and shedding occur simultaneously in eucalypt canopies (Duursma et al. 2016; Pook 1984), the overall canopy volume can remain stable while the distribution of canopy volume changes with height (Griebel et al. 2015). Eucalypt forests in southeast Australia have been found to act as carbon sinks all year long, with greater uptake in summer (Hinko-Najera et al. 2017; van Gorsel et al. 2013). Although canopy characteristics are key to understanding ecosystem fluxes, their dynamics in Australian ecosystems can be particularly challenging to detect using standard vegetation indices (Moore et al. 2016). Nevertheless, the normalized difference vegetation index (NDVI) has successfully explained variability in photosynthetic capacity in Mediterranean, mulga and savanna ecosystems (Restrepo-Coupe et al. 2016).

80 The environmental and biotic controls on the seasonal dynamics of ecosystem fluxes in broadleaved  
81 evergreen forests are still poorly understood. Our objective was to determine the seasonality of  
82 ecosystem CO<sub>2</sub> and H<sub>2</sub>O fluxes in a dry sclerophyll Eucalyptus forest; we evaluated the role of  
83 environmental drivers (PPFD, T<sub>a</sub>, SWC and D) and canopy dynamics (as measured with EVI, LAI,  
84 litter fall and leaf age) in regulating the seasonal patterns of net ecosystem exchange (NEE), gross  
85 primary productivity (GPP), ecosystem respiration (ER), evapotranspiration (ET) and surface  
86 conductance (G<sub>s</sub>) in an evergreen forest near Sydney, Australia. We also compared leaf-level to  
87 ecosystem-level water and carbon exchange in response to drivers, in order to gain confidence in our  
88 results and gain insights about the emergent properties from leaf to ecosystem scale. We hypothesised  
89 that canopy phenology (LAI and leaf age) explains temporal variation in photosynthetic capacity (PC)  
90 and G<sub>s</sub>. We anticipated that the ecosystem would be a carbon sink all year long.

## 91 2. Material and methods

### 92 2.1 Site description

93 The field site is the Cumberland Plain (AU-Cum in Fluxnet) forest SuperSite (Resco de Dios et al.  
94 2015) of the Australian Terrestrial Ecosystem Research Network (<http://www.ozflux.org.au>), located  
95 50 km west of Sydney, Australia, at 19 m elevation, on a nearly flat floodplain of the Nepean-  
96 Hawkesbury River (latitude -33.61320; longitude 150.72446). Mean mid-afternoon (3 pm)  
97 temperature is 18 °C (max. 28.5 °C in January and min. 16.5 °C in July) and average precipitation is  
98 801 mm year<sup>-1</sup> (mean monthly max. is 96 mm in January, and min. is 42 mm in September). The soil  
99 is classified as a Kandosol and consists of a fine sandy loam A horizon (0-8 cm) over clay to clay  
100 loam subsoil (8-40 cm), with pH of 5 to 6 and up to 5% organic C in the top 10 cm (Karan et al.  
101 2016). The flux tower is in a mature dry sclerophyll forest, with 140 Mg C ha<sup>-1</sup> aboveground biomass  
102 and stand density of ~500 trees ha<sup>-1</sup>. The stand hosts a large population of mistletoe (*Amyema*  
103 *miquelii*), which decreases in abundance with increasing distance to the flux tower. The canopy  
104 structure comprises three strata, and the predominant canopy tree species are *Eucalyptus moluccana*  
105 and *E. fibrosa*. While individual trees can exceed 25 m height, an airborne LiDAR survey from  
106 November 2015 indicates an average canopy height of ~24 m within a 300 m radius of the flux tower  
107 (supplement figure S1). The mid-canopy stratum (5-12 m) is dominated by *Melaleuca decora* and the  
108 understory is dominated by *Bursaria spinosa* with various shrubs, forbs, grasses and ferns present in  
109 lower abundance.

### 110 2.2 Environmental measurements

111 Air temperature ( $T_a$ ) and relative humidity (RH) were measured using HMP45C (Vaisala, Vantaa,  
112 Finland) sensors at 7 m and 29 m heights. Vapour pressure deficit (D) was estimated from  $T_a$  and RH.  
113 Photosynthetic photon flux density above the canopy (PPFD,  $\mu\text{mol m}^{-2} \text{s}^{-1}$ ) was measured using an  
114 LI190SB (Licor Inc., Lincoln NE, USA), and incoming and outgoing short and longwave radiation  
115 were measured using a CNR1 radiometer (Kipp & Zonen, Delft, Netherlands). Ancillary data were  
116 logged on CR1000 or CR3000 dataloggers (Campbell Scientific, Logan UT, USA) at 30 min  
117 intervals. Mixing ratios of CO<sub>2</sub> in air were also measured at 0.5 m, 1 m, 2 m, 3.5 m, 7 m, 12 m, 20 m,  
118 and 29 m above the soil surface using a LI840A Gas Analyzer (Licor Inc., Lincoln NE, USA); data  
119 from each height were logged on a CR1000 datalogger once every 30 minutes (1 minute air sampling  
120 per height).

121 Ground heat flux and soil moisture were averaged between two locations to represent the variable  
122 shading in the tower footprint. One location had a HFP01 heat flux plate and the other had a self-  
123 calibrating heat flux plate (HFP01SC) (Hukseflux, XJ Delft, Netherlands) installed at 8 cm below the  
124 soil surface. The heat flux plates were paired with a CS616 water content reflectometer (Campbell  
125 Scientific, Logan UT) installed horizontally at 5 cm below the soil surface and a TCAV averaging  
126 thermocouple (Campbell Scientific, Logan UT) installed with thermocouples at 2 cm and 6 cm below  
127 the soil surface for each pair. A CS616 installed vertically measured average soil water content from 7  
128 to 37 cm (CS616). Rainfall was measured at an open area with a tipping bucket 2 km away from the  
129 study site.

### 130 2.3 Net ecosystem exchange

131 Continuous land-atmosphere exchange of CO<sub>2</sub> mass (net ecosystem exchange, NEE) was quantified  
132 from direct measurements of the different components of the theoretical mass balance of CO<sub>2</sub> in a  
133 control volume:

$$NEE = F_{CT} + F_{CS} \quad (1)$$

134 Where  $F_{CT}$  is the vertical turbulent exchange flux, and  $F_{CS}$  is the change in storage flux. Advection  
 135 fluxes are assumed negligible when atmospheric turbulence is sufficient (Aubinet et al. 2012;  
 136 Baldocchi et al. 1988), and when quality flags of stationarity and turbulence development test were  
 137 good (Foken et al. 2004). We used change-point detection of the friction velocity ( $u^*$ ) threshold (Barr  
 138 et al. 2013) to determine the turbulence threshold above which NEE (the sum of  $F_{CT}$  and  $F_{CS}$ ) is  
 139 independent of  $u^*$ . However, we found no clear dependence of NEE on  $u^*$  hence no clear threshold  
 140 (Figure S2), so we used a threshold of  $0.2 \text{ m s}^{-1}$  to be conservative.

141 The calculation of each term, and the assumptions required for them to be representative of each half-  
 142 hour flux are detailed below.

#### 143 2.4 Vertical turbulent flux ( $F_{CT}$ )

144 The vertical turbulent fluxes of  $\text{CO}_2$  ( $F_{CT}$ ,  $\mu\text{mol m}^{-2} \text{ s}^{-1}$ ) and water ( $F_{WT}$ ,  $\text{mmol m}^{-2} \text{ s}^{-1}$ ) were measured  
 145 using the eddy-covariance method (Baldocchi et al. 1988). Density ( $c$ ) of  $\text{CO}_2$  or water vapor (open-  
 146 path IRGA (LI-7500A, Licor Inc., Lincoln NE, USA)) and vertical wind speed ( $w$ ) (CSAT 3D sonic  
 147 anemometer (Campbell Scientific, Logan UT, USA)) were measured at 10 Hz frequency at 29 m  
 148 above the ground, and logged on a CR-3000 datalogger (Campbell Scientific, Logan UT, USA).  
 149 Vertical turbulent fluxes were calculated from the 10 Hz data, using Eddy-Pro© software. Statistical  
 150 tests for raw data screening followed (Vickers and Mahrt 1997), including spike count/removal,  
 151 amplitude resolution, drop-outs, absolute limits and skewness and kurtosis tests. Low and high  
 152 frequency spectral correction followed (Moncrieff et al. 2004), and (Moncrieff et al. 1997). The  
 153 calculation allowed for up to 10% of missing 10 Hz data. Fluxes were rotated into the natural wind  
 154 coordinate system using the double rotation method (Wilczak et al. 2001). Time lags between the  
 155 sonic and IRGA were compensated using covariance maximization, within a window of plausible  
 156 time lags (Fan et al. 1990). We applied the block averaging method to calculate each half-hour  
 157 average and fluctuation relative to the average, to calculate the covariance (Gash and Culf 1996).  
 158 Density fluctuations in the air volume were corrected using the WPL terms (Webb et al. 1980). Each  
 159 half-hourly flux was associated with a quality flag (0: good quality, 1: keep for integrations, discard  
 160 for empirical relationships, 2: remove from the data); these flags accounted for stationarity tests and  
 161 turbulence development tests which are required for good turbulent flux measurements (Foken et al.  
 162 2004). In our 4-year record, 51% of  $F_{CT}$  fluxes had a flag of 0, 32% had a flag of 1 and 17% had a flag  
 163 of 2. Although the tower height (29m) is rather close to the average canopy height (24m), cospectra  
 164 analysis showed good quality turbulent fluxes (the high frequency followed the  $-4/3$  slope, thus we  
 165 did not find any indications of systematic dampening in the cospectra, see figure S3).

#### 166 2.5 Storage flux ( $F_{CS}$ )

167 The change in storage flux ( $F_{CS}$ ,  $\mu\text{mol m}^{-2} \text{ s}^{-1}$ ) was measured using a  $\text{CO}_2$  profiler system, such that  
 168 change of storage flux timestamp was the same as the turbulent flux timestamp. The change in storage  
 169 flux was calculated as (Aubinet et al. 2001):

$$F_{CS} = \frac{P_a}{R T_a} \int_0^h \frac{dC(z)}{dt} dz \quad (2)$$

170 Where  $P_a$  is the atmospheric pressure ( $P_a$ ),  $T_a$  is the temperature (K),  $R$  is the molar gas constant, and  
 171  $C(z)$  is  $\text{CO}_2$  ( $\mu\text{mol m}^{-3}$ ) at the height  $z$ .  $\text{CO}_2$  is measured in ppm and converted to  $\mu\text{mol m}^{-3}$  using ideal  
 172 gas law equation, where the air temperature and air pressure at each inlet is estimated from a linear  
 173 interpolation between sensors at the top of the tower (29m) and sensors at the bottom of the tower  
 174 (7m). As we only measure a limited number of heights, this equation becomes, in practice:

$$F_{CS} = \left(\frac{\Delta C}{\Delta t}\right)_{k=1} \times z_{k=1} + \sum_{k=2}^n \left\{ \left[ \left(\frac{\Delta C}{\Delta t}\right)_k + \left(\frac{\Delta C}{\Delta t}\right)_{k-1} \right] \times \frac{z_k - z_{k-1}}{2} \right\} \quad (3)$$

175 Where C is CO<sub>2</sub> (μmol m<sup>-3</sup>) and t is time (s) (ΔC/Δt is the variation of C over 30 minutes), z is the  
 176 height (m), k [1 to n = 8] represents each inlet. We flagged and replaced the storage flux with a one-  
 177 point approximation during profiler outages (25% of the 4-year record), using the change in CO<sub>2</sub> at 29  
 178 m height over 30 minutes as derived in EddyPro (Aubinet et al. 2001). These data were not used for  
 179 empirical relationships, but kept for annual sum calculations. Storage flux of water vapour was  
 180 assumed to be negligible. For visualisation of the diurnal course of storage flux and turbulent flux, see  
 181 Figure S4.

## 182 2.6 Gap-filling of environmental variables and NEE separation into gross fluxes

183 We used the PyFluxPro software for gap-filling climatic variables and fluxes, and for partitioning the  
 184 NEE into gross primary productivity (GPP) and ecosystem respiration (ER) (Isaac et al. 2017). We  
 185 only used observational data that passed the steady state and developed turbulence tests for gap-filling  
 186 and for partitioning (QC flags of 0 and 1; (Foken et al. 2004)). In brief, gaps in climate variables were  
 187 filled following the hierarchy of using variables provided from 1) automatic weather stations from the  
 188 closest weather station, 2) numerical weather prediction model outputs (ACCESS regional, 12.5 km  
 189 grid size provided by the Bureau of Meteorology) and lastly 3) monthly mean values from the site-  
 190 specific climatology. In a next step the continuous climate variables were used to fill all fluxes by  
 191 utilizing the embedded SOLO neural network with 25 nodes and 500 iterations on monthly windows.  
 192 We used ‘Random Forest’ (Breiman 2001) to determine and rank potential explanatory variables for  
 193 explaining latent heat flux (λE), sensible heat flux (H) and NEE. We then selected the five variables  
 194 with the highest feature importance for each flux and compared the gap-filling performance of the  
 195 neural network for each flux with the performance based on an educated guess of potential relevant  
 196 drivers. We selected the variable array with the highest Pearson correlation coefficient (r) and lowest  
 197 root mean square error (RMSE) for gap-filling in PyFluxPro, which identified net radiation (R<sub>n</sub>), soil  
 198 water content (SWC), soil temperature (T<sub>s</sub>), wind speed (w<sub>s</sub>) and vapor pressure deficit (D) for λE (r =  
 199 0.93, RMSE = 32.0); down-welling shortwave radiation (F<sub>sd</sub>), air temperature (T<sub>a</sub>), T<sub>s</sub>, w<sub>s</sub>, SWC and  
 200 D for H (r = 0.97, RMSE = 23.1) and F<sub>sd</sub>, D, T<sub>a</sub>, T<sub>s</sub> and SWC for NEE (r = 0.87, RMSE = 4.04). To  
 201 gap-fill ER, all nocturnal observational data (at night, we assume GPP = 0 so NEE = ER) that passed  
 202 all quality control checks and the u\*-filter were modelled using T<sub>s</sub>, T<sub>a</sub> and SWC as drivers in SOLO  
 203 on the full dataset with 10 nodes and 500 iterations. Lastly, this gap-filled ER was used to infer GPP  
 204 as the result of NEE - ER.

## 205 2.7 Flux footprint

206 We analysed the footprint climatology of AU-Cum site according to (Kormann and Meixner 2001),  
 207 using the R-Package ‘FREddyPro’ (Figure S5). We assumed that the ecosystem within the footprint  
 208 was homogeneous for the purpose of this study.

## 209 2.8 Energy balance

210 We evaluated the energy balance closure with the ratio of available energy (R<sub>n</sub> – soil heat flux (G)) to  
 211 the sum of turbulent heat fluxes (λE + H). On a daily basis, the energy balance closure was 70%  
 212 (Figure S6), consistent with the well-known and common issue of a lack of closure (Foken 2008;  
 213 Foken et al. 2006; Wilson et al. 2002). We did not use the criteria that closure had to be met for the  
 214 reported fluxes.

215 *2.9 Surface conductance*

216 Surface conductance ( $G_s$ ) was derived by inverting the Penman-Monteith equation (Monteith 1965):

$$G_s = \frac{\gamma \lambda E g_a}{\Delta R_n + \rho C_p D g_a - \lambda E (\Delta + \gamma)} \quad (4)$$

217 Where  $\gamma$  is the temperature dependent psychrometric constant ( $\text{kPa K}^{-1}$ ),  $\lambda E$  is the latent heat flux ( $\text{W m}^{-2}$ ),  $\Delta$  is the temperature dependent slope of the saturation-vapor pressure curve ( $\text{kPa K}^{-1}$ ),  $R_n$  is net radiation ( $\text{W m}^{-2}$ ),  $\rho$  is the dry air density ( $\text{kg m}^{-3}$ ),  $D$  is vapor pressure deficit ( $\text{kPa}$ ),  $C_p$  is the specific heat of air ( $\text{J kg}^{-1} \text{K}^{-1}$ ), and  $g_a$  is the bulk aerodynamic conductance, formulated as an empirical relation of wind speed ( $w_s$ ,  $\text{m s}^{-1}$ ) and friction velocity ( $u^*$ ,  $\text{m s}^{-1}$ ) (Thom 1972):

$$g_a = \frac{1}{\frac{w_s}{u^{*2}} + 6.2 u^{*-0.67}} \quad (5)$$

222 In the analysis for  $G_s$ , we were interested in transpiration (T) rather than evaporation (E), so we  
 223 excluded data if precipitation exceeded 1 mm in the past 2 days, 0.5 mm in the past 24 hours, and 0.2  
 224 mm in the past 12 hours (Knauer et al. 2015). We assumed that evaporation (E) is negligible using  
 225 these criteria (Knauer et al. 2017), which excluded 40% of the data.

226 *2.10 Potential evapotranspiration*

227 Potential evapotranspiration rate (PET) was derived using Penman-Monteith equation (Monteith  
 228 1965):

$$PET = \frac{\Delta R_n + C_p \rho G_a D}{\gamma [\Delta + \gamma(1 + \frac{G_a}{G_{s,max}})]} \quad (6)$$

229 where  $G_{s,max}$  is the well-watered reference surface conductance, calculated as the average of  $G_s$  at the  
 230 study site when soil moisture exceeds the 75% quantile and  $D$  is above 0.9 and below 1.1 kPa (Novick  
 231 et al. 2016).

232 *2.11 Dynamics of canopy phenology (leaf area index, litter and leaf production) and  
 233 photosynthetic capacity*

234 We evaluated the dynamics of canopy leaf area index (LAI) by measuring canopy light transmittance  
 235 with three under-canopy PPFD sensors and one above canopy PPFD sensor LI190SB (Licor Inc.,  
 236 Lincoln NE, USA) following the methods presented in (Duursma et al. 2016). Although we use the  
 237 term LAI, this estimate does include non-leaf surface area (stems, branches). We collected litterfall  
 238 ( $L_f$ ,  $\text{g m}^2 \text{month}^{-1}$ ) in the tower footprint approximately once per month, from nine litter traps ( $0.14 \text{ m}^2$   
 239 ground area) located near the understory PPFD sensors. We estimated specific leaf area (SLA) of  
 240 Eucalyptus and mistletoe leaves by sampling approximately 50 fresh leaves of each, in June 2017  
 241 (SLA =  $56.4 \text{ cm}^2 \text{g}^{-1}$  for eucalyptus,  $40.3 \text{ cm}^2 \text{g}^{-1}$  for mistletoe). For each month, we partitioned the  
 242 litter into Eucalyptus leaves, mistletoe leaves, and other (mostly woody) components. We used this  
 243 SLA to estimate leaf litter production ( $L_p$ ) in  $\text{m}^2 \text{m}^{-2} \text{month}^{-1}$  of eucalyptus, mistletoe, and total as the  
 244 sum of both. Then, we estimated leaf growth ( $L_g$ ,  $\text{m}^2 \text{month}^{-2}$ ) as the sum of the net change in LAI  
 245 ( $\Delta L$ ) and  $L_p$ . Photosynthetic capacity (PC) is defined as median GPP when PPFD is 800-1200  $\mu\text{mol}$   
 246  $\text{m}^{-2} \text{s}^{-1}$  and  $D$  is 1.0 to 1.5 kPa.

247 *2.12 Analysis of light-response of NEE*

248 We evaluated the light response of NEE using a saturating exponential function (Eq. 5) to test whether  
249 parameters varied between seasons (Aubinet et al. 2001; Lindroth et al. 2008; Mitscherlich 1909).

$$NEE = -(NEE_{sat} + R_d) \left( 1 - \exp \left[ \frac{-\alpha PPF D}{NEE_{sat} + R_d} \right] \right) + R_d \quad (7)$$

250 where the parameter  $R_d$  is the intercept, or NEE in the absence of light, often called dark respiration;  
251  $NEE_{sat}$  is NEE at light saturation and  $\alpha$  is the initial slope of the curve, expressed in  $\mu\text{mol CO}_2 \mu\text{mol}$   
252  $\text{photon}^{-1}$  and representing light use efficiency when photosynthetic photon flux density (PPFD) is  
253 close to 0. We only used daytime quality checked NEE data to fit the model ( $qc = 0$ ; (Foken et al.  
254 2004), LI-7500 signal strength = max, all inlets of profiler system data available and  $u^* > 0.2 \text{ m s}^{-1}$ ),  
255 see Figure S7.

256 *2.13 Leaf gas exchange spot measurements*

257 We used previously published data of spot leaf gas exchange measurements in a nearby site for  
258 comparison with ecosystem fluxes (Gimeno et al. 2016).



### 3. Results

#### 260 3.1 Seasonality of environmental drivers and leaf area index

261 Climatic conditions were favorable for growth at the site year-round. The monthly average of daily  
 262 maximum air temperature was 16.3 °C during the coldest month (July 2015), and the lowest monthly  
 263 average of daily maximum PPFD was 878  $\mu\text{mol m}^{-2} \text{s}^{-1}$  in the winter (June 2015; Figure 1c). Although  
 264 less rainfall occurred during winter months compared to summer months, precipitation occurred  
 265 throughout the year (Figure 1b). Soil volumetric water content in the shallow (0-8 cm) layer was  
 266 about 10% except immediately following rain events (Figure 1b). In contrast, soil water content in the  
 267 clay layer (8 -38cm) remained above 30% for the duration of the study (data not shown). Monthly  
 268 average of daily maximum air temperature ranged from 16.3 °C in July 2015 to 32.7 °C in January  
 269 2017; monthly average of daily maximum D ranged from 0.9 kPa in June 2015 to 3.4 kPa in January  
 270 2017 (Figure 1c). For visualisation of seasonal and diurnal trends of radiation, air temperature, D and  
 271 SWC, see supplement Figure S8.

272 Canopy leaf area index varied between 0.7 (in December 2014) and 1.1  $\text{m}^2 \text{m}^{-2}$  (in February 2015)  
 273 (Figure 1d). LAI followed a distinct pattern: it peaked in late summer (around January), and then  
 274 continuously decreased until the new leaves emerged the following year. A late leaf flush was  
 275 observed in 2017 (April). Litter production was concurrent with leaf growth and also peaked in  
 276 summer, before and during the leaf flush, and was lower in winter (Figure 1d).

#### 277 3.2 Seasonality of carbon and water fluxes

278 Contrary to expectations, the ecosystem was always a sink for carbon in winter (-146  $\text{g C m}^{-2}$  on  
 279 average, with a standard deviation of 22  $\text{g C m}^{-2}$ ), and usually a carbon source or close to neutral in  
 280 summer (+ 44  $\text{g C m}^{-2}$  on average, with a standard deviation of 43  $\text{g C m}^{-2}$ ) (Table 1). On average,  
 281 summer GPP was lower – i.e. more uptake (-400  $\pm$  97  $\text{g C m}^{-2}$ ) compared to winter GPP (-282  $\pm$  41  $\text{g}$   
 282  $\text{C m}^{-2}$ ) (Table 1), that is a difference of  $\sim$  118  $\text{g C m}^{-2}$ . However, average summer ER was much  
 283 higher (444  $\pm$  56  $\text{g C m}^{-2}$ ) compared to winter ER (159  $\pm$  35  $\text{g C m}^{-2}$ ) (Table 1), a difference of  $\sim$  285  
 284  $\text{g C m}^{-2}$ . The summer vs. winter ER difference was more than double the GPP difference; thus, ER  
 285 had a relatively larger effect over the seasonality of NEE.

#### 286 3.3 Diurnal trend of $\text{CO}_2$ flux and drivers in winter and summer

287 The diurnal pattern of NEE in clear-sky conditions differed between summer and winter (Figure 2).  
 288 Relatively speaking, diurnal NEE was more symmetric in the winter than in summer. That is, morning  
 289 and afternoon NEE pattern resembled a mirror image and total integrated morning NEE was similar to  
 290 integrated afternoon NEE during the winter, but strong hysteresis occurred in the summer (Figure 2).  
 291 This pattern also translated into hysteresis in the NEE light response curve in summer, but to a lesser  
 292 degree in winter (Figure 3).

#### 293 3.4 Analysis of NEE light response curve

294 The parameters of the NEE light response in summer and winter are shown in Figure 4 (see methods,  
 295 Eq. 5). The initial slope of NEE with light ( $\alpha$ ) showed no clear dependence on  $T_{\text{soil}}$  in winter but  
 296 exhibited sensitivity during summer, dropping precipitously at soil temperature above 23 °C (Figure  
 297 4a).  $\alpha$  increased with SWC in winter and summer by a factor of 1.5 (Figure 4b). In both winter and  
 298 summer  $\alpha$  decreased with D ( $D > 1$  kPa) and in a similar fashion, approaching a saturating value of  
 299 0.01 ( $\mu\text{mol } \mu\text{mol}^{-1}$ ) at a D of about 2 kPa (Figure 4c). The fitted NEE at saturating light ( $\text{NEE}_{\text{sat}}$ ) was  
 300 not related to  $T_{\text{soil}}$  in winter but decreased with increasing  $T_{\text{soil}}$  in summer (Figure 4d).  $\text{NEE}_{\text{sat}}$  was  
 301 higher in winter than in summer for a given SWC. The relationship with D was more complicated,  
 302 tending to increase with D in winter, but decreasing with increased D in summer, dropping from 9 to

303 3 ( $\mu\text{mol m}^{-2} \text{s}^{-1}$ ) as D increased from 1 to 4 kPa.  $R_d$  was significantly higher in summer than winter  
304 across all conditions of  $T_{\text{soil}}$ , SWC and D (Figure 4g, h, i).  $R_d$  increased with  $T_{\text{soil}}$  in winter and less so  
305 in summer. In winter,  $R_d$  increased up to SWC of 11%; in summer,  $R_d$  was more sensitive to SWC,  
306 doubling from a rate of  $\sim 4$  to  $\sim 8 \mu\text{mol m}^{-2} \text{s}^{-1}$  as SWC increased from about 8 to 20%.

### 307 3.5 Atmospheric demand and soil drought control on GPP, ET, $G_s$ and WUE

308 We evaluated the effect of soil water content (SWC at 0-8 cm depth) and vapour pressure deficit (D)  
309 on GPP, ET, water use efficiency (WUE) and canopy conductance ( $G_s$ ) under high radiation (“light-  
310 saturated”; PPFD  $> 1000 \mu\text{mol m}^{-2} \text{s}^{-1}$ ), after filtering periods following rain events in order to  
311 minimise the contribution of evaporation to ET (see Methods) (Figure 5). In summer, light-saturated  
312 GPP decreased above D  $\sim 1.3$  kPa, but in winter, GPP did not vary with D. In summer and in winter,  
313 GPP increased with SWC (Figure 5a). This is consistent with Figure 4, where  $R_d$  and  $NEE_{\text{sat}}$  both  
314 increased with SWC. In summer, light-saturated ET increased with D up to  $\sim 1.3$  kPa, above which it  
315 reached a plateau. In winter, ET kept increasing with D, as D rarely exceeded 2 kPa. In both seasons,  
316 ET increased with SWC (Figure 5b). Surface conductance decreased with D and SWC especially in  
317 summer, indicating strong stomatal regulation (Figure 5d). Water use efficiency (WUE) decreased  
318 with increasing D in summer and in winter, because ET increased but -GPP declined (Figure 5c).

319 We compared these ecosystem-scale results to the equivalent at the leaf-scale, which are net  
320 photosynthesis at light saturation  $A_{\text{max}}$  (PPFD  $\sim 1800 \mu\text{mol m}^{-2} \text{s}^{-1}$ ), leaf transpiration T, leaf water use  
321 efficiency, and stomatal conductance  $g_s$  (Figure 5, black lines). These leaf level measurements are  
322 expressed on a leaf-area basis, as compared to ground area for ecosystem scale. We observed that  
323  $A_{\text{max}}$ , T and  $g_s$  were more sensitive to D than corresponding ecosystem-scale responses.  $A_{\text{max}}$  was  
324 much higher than  $GPP_{\text{max}}$  at D  $\sim 1$  kPa, while  $g_s$  was comparable in magnitude to  $G_s$  in the same  
325 condition. Leaf transpiration peaked around D = 1.2 kPa, while ET plateaued. Leaf water use  
326 efficiency was overall higher than ecosystem WUE.

### 327 3.6 Canopy phenology control of GPP

328 Monthly average photosynthetic capacity (PC) varied by a factor of  $\sim 2$  across the study period,  
329 ranging from  $8.4 \mu\text{mol m}^{-2} \text{s}^{-1}$  before the leaf flush in November 2014 to  $15 \mu\text{mol m}^{-2} \text{s}^{-1}$  after the leaf  
330 flush occurred in March 2016. We expected that PC could be predicted by LAI, EVI and  $G_s$ . Leaf area  
331 index (LAI) and photosynthetic capacity (PC) were significantly correlated; the slope was  
332 significantly different from zero ( $r^2 = 0.24$ ,  $p < 0.005$ ,  $PC = 8.8 \text{ LAI} + 3.7$ , Figure 6). EVI was even  
333 more significantly correlated with PC ( $r^2 = 0.46$ ,  $p < 0.005$ ,  $PC = 52 \text{ EVI} - 5.3$ , Figure 6).  $G_{s,\text{max}}$  was  
334 significantly correlated with PC ( $r^2 = 0.2$ ,  $p < 0.005$ ,  $PC = 9 G_{s,\text{max}} + 9$ ) and LAI ( $r^2 = 0.27$ ,  $p < 0.005$ ,  
335  $G_{s,\text{max}} = 0.51 \text{ LAI} - 0.17$ ) and with EVI ( $r^2 = 0.29$ ,  $p < 0.005$ ,  $G_{s,\text{max}} = 2.3 \text{ EVI} - 0.45$ ). The  
336 correlations with NDVI were less significant than with EVI (see figure S9).

#### 4. Discussion

We measured four consecutive years of carbon, water and energy fluxes in a native evergreen broadleaf Eucalyptus forest, including canopy dynamics and environmental drivers (photosynthetically active radiation, air and soil temperature, precipitation, soil water content, and atmospheric demand). We hypothesised that the Cumberland Plain forest would be a carbon sink all year-round, similar to other eucalypt forests (Beringer et al. 2016; Hinko-Najera et al. 2017; Keith et al. 2012). We also hypothesised higher net carbon uptake during summer, due to warmer temperatures, higher light and longer day length contributing to higher photosynthesis, compared to winter. However, the site was a net source of carbon during summer, and a net sink of carbon during winter.

The seasonal pattern of NEE was driven mostly by ER, as the seasonal amplitude of ER was larger than the seasonal amplitude of GPP. The seasonality of ER may be explained by the positive effects of higher temperatures on the rates of autotrophic respiration (Tjoelker et al. 2001), and on the activity of microbes to increase soil organic matter decomposition (Lloyd and Taylor 1994); low soil moisture in the shallow layers sometimes limited decomposition (January and February 2014, January and December 2015, February and December 2017, see Figure 1), but often regular rainfall maintained adequate soil moisture. The relatively low seasonality of GPP may be partly explained by lower photosynthetic capacity in early summer (before January) when LAI was at its lowest, and the leaves have reached maximum age because new leaves have not yet emerged. The ER-driven seasonality of NEE is in sharp contrast with cold temperate forests where GPP drives the seasonality of NEE. ER-driven NEE seasonality was also observed in an Asian tropical rain forest, as ER was higher than GPP in the rainy season leading to net ecosystem carbon loss, while in the dry season, ecosystem carbon uptake was positive (Zhang et al. 2010). This pattern was also observed in an Amazon tropical forest (Saleska et al. 2003).

A strong morning-afternoon hysteresis of NEE response to PPFD occurred in summer, and less so in winter (Figure 3). In winter, low D and moderately warm daytime air temperatures and high PPFD were sufficient to maintain high photosynthesis rates throughout most of the day (Figure 1). In summer, two possible explanations of the diurnal hysteresis of NEE are (1) ER is greater in the afternoon compared to morning or (2) GPP is lower in the afternoon compared to morning. Explanation (1) is plausible, as temperature drives autotrophic and heterotrophic respiration; however, it is unlikely to explain the hysteresis magnitude which is higher in summer compared to winter. Explanation (2) could arise from lower afternoon stomatal conductance or lower photosynthetic capacity (e.g. the maximum rate of carboxylation ( $V_{cmax}$ ) decreases at high  $T_a$ ), or a combination of both or even circadian regulation (Jones et al. 1998; Resco de Dios et al. 2015). An analysis of surface conductance showed strong stomatal regulation (Figure 2, Figure 3, Figure 5), induced by high atmospheric demand and high air temperature (Duursma et al. 2014), limiting photosynthesis during the afternoon of warm months (see Figure S10). These diurnal patterns of NEE, GPP and ER play a strong role in regulating the seasonal carbon cycling dynamics in this ecosystem. A wavelet coherence analysis between D and GPP showed strong coherence at seasonal time scale (periods of three months), see figure S11.

We observed comparable responses of leaf-level and ecosystem-level gas exchange to environmental drivers (Figure 5). The larger magnitude of  $A_{max}$  than GPP at high D may be explained by the proportion of shaded leaves in the ecosystem. The similar magnitude for  $G_s$  and  $g_s$  was also expected, as LAI is close to 1 and  $R_n$  is not a driver for stomatal conductance. The peaked pattern of T versus D, as opposite to saturating pattern of ET, may be explained by (1) the contribution of soil evaporation to

382 ET or (2) the presence of mistletoe, known for not regulating their stomata (Griebel et al. 2017). The  
383 higher magnitude of leaf water use efficiency results from the combination of higher  $A_{\max}$  and similar  
384 or lower leaf transpiration compared to ET. Furthermore, we compared leaf level  $g_1$  and ecosystem  
385 level  $G_1$ , using the optimal stomatal conductance model (Medlyn et al. 2011):  $G_1$  was lower than  $g_1$   
386 ( $1.6 \pm 0.06$  for  $G_1$ ,  $4.4 \pm 0.2$  for  $g_1$ , see figure S12).

387 Our study demonstrated that canopy dynamics (specifically, LAI in our study) play an important role  
388 in regulating seasonal variations in GPP even in evergreen forests. Similar observations emerged from  
389 a tropical forest, where leaf area index and leaf age explained the seasonal variability of GPP (Wilson  
390 et al. 2001; Wu et al. 2016), as the photosynthetic capacity (PC, the maximum rate of GPP in optimal  
391 environmental condition) varied with leaf age. In Australian woodlands, PC ( $A_{\max}$ ) of leaves was also  
392 found to decrease with leaf age,  $A_{\max}$  declined by 30% on average between young and old leaves, for  
393 10 different species (Reich et al. 2009). In the Cumberland Plain forest, periods with high LAI co-  
394 occur with mature, efficient leaves, and periods with low LAI co-occur with old, less efficient leaves.  
395 LAI was correlated with PC, which was probably the result of both a greater number of leaves and  
396 more efficient leaves. Remotely sensed vegetation indices such as (EVI) or (NDVI) assess whether  
397 the target being observed contains live green vegetation. In Australia, NDVI and EVI were good  
398 predictors of photosynthetic capacity in savanna, mulga and Mediterranean-mallee ecosystems  
399 (Restrepo-Coupe et al. 2016). For our site, EVI was a good predictor of PC, which was surprising as  
400 satellite-derived LAI values have been found to be typically inaccurate in open forests and forests in  
401 southeast Australia (Hill et al. 2006). NDVI was a poor predictor of PC (see figure S9).

402 In a global study, it was shown that mean annual NEE decreased with increasing dryness index  
403 (PET/P) in sites located below  $45^\circ$  N latitude (Yi et al. 2010). It has also been shown that *Eucalyptus*  
404 grow more slowly in warm environments (Prior and Bowman 2014). At our site, and in a previous  
405 study in *Eucalyptus* forest (van Gorsel et al. 2013), GPP decreased with D above a threshold of  $\sim 1.3$   
406 kPa. Our results indicate that surface conductance ( $G_s$ ) decreased above that threshold, suggesting that  
407 the decrease in GPP is caused by stomatal regulation. As D correlates with air temperature, it is  
408 difficult to distinguish the relative contribution of D and  $T_a$  to the decrease of  $G_s$ , but they are thought  
409 to both impact  $G_s$  (Duursma et al. 2014). Cumberland Plain has the highest mean annual temperature  
410 and the highest dryness index among the four *Eucalyptus* forest eddy-covariance sites in south-east  
411 Australia (Beringer et al. 2016), which could explain its strong sensitivity to D and hence its unique  
412 seasonality.

## 413 **5. Conclusions**

414 The Cumberland Plain forest was a net C source in summer and a net C sink in winter, in contrast to  
415 other Australian eucalypt forests which were net C sinks year-round. ER drove NEE seasonality, as  
416 the seasonal amplitude of ER was greater than GPP. ER was high in the warmer, wetter months of  
417 summer, when environmental conditions supported high autotrophic respiration and heterotrophic  
418 decomposition. Meanwhile, GPP was limited by lower LAI and probably older leaves in early  
419 summer, and by high D which limited  $G_s$  throughout the summer. Despite being evergreen, there was  
420 significant temporal variation in LAI, which was correlated with monthly photosynthetic capacity and  
421 monthly surface conductance. Understanding LAI dynamics and its response to precipitation regimes  
422 will play a key-role in climate change feedback.

## 423 **Code and data availability**

424 All the datasets and scripts used in this manuscript can be downloaded at:  
425 <http://doi.org/10.5281/zenodo.1219977>

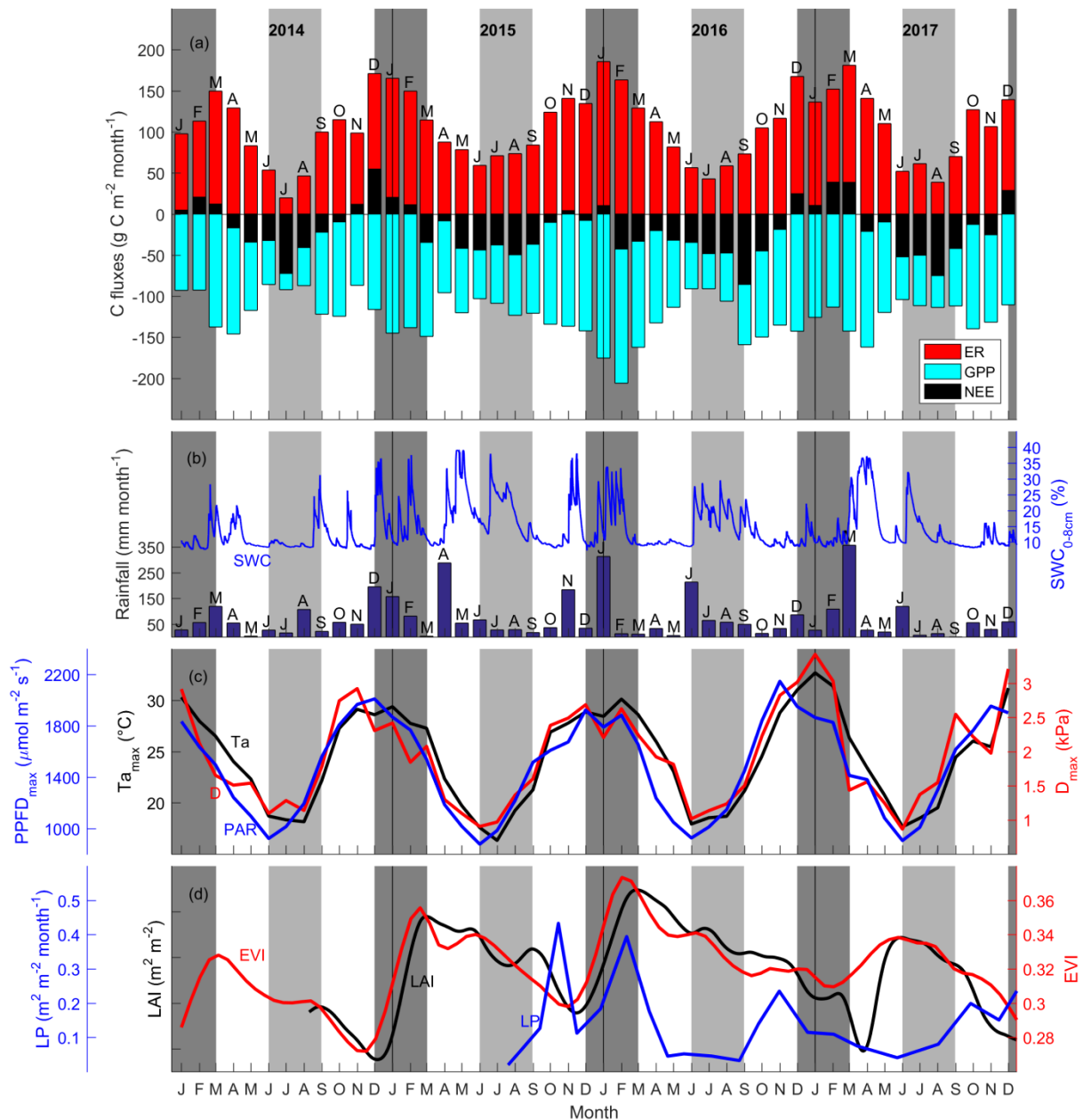
## 426 **Author contribution**

427 DT, VRD, EP, AAR conceived the project; CVMB, CM, EP, AAR, AG, MMB, DM collected the  
428 data and assured the maintenance of the experiment; AAR, AG, DM, CAW, EP, PI, VRD, analysed  
429 the data; AAR, EP, VRD wrote the manuscript with input from all other authors.

430 The authors declare that they have no conflict of interest.

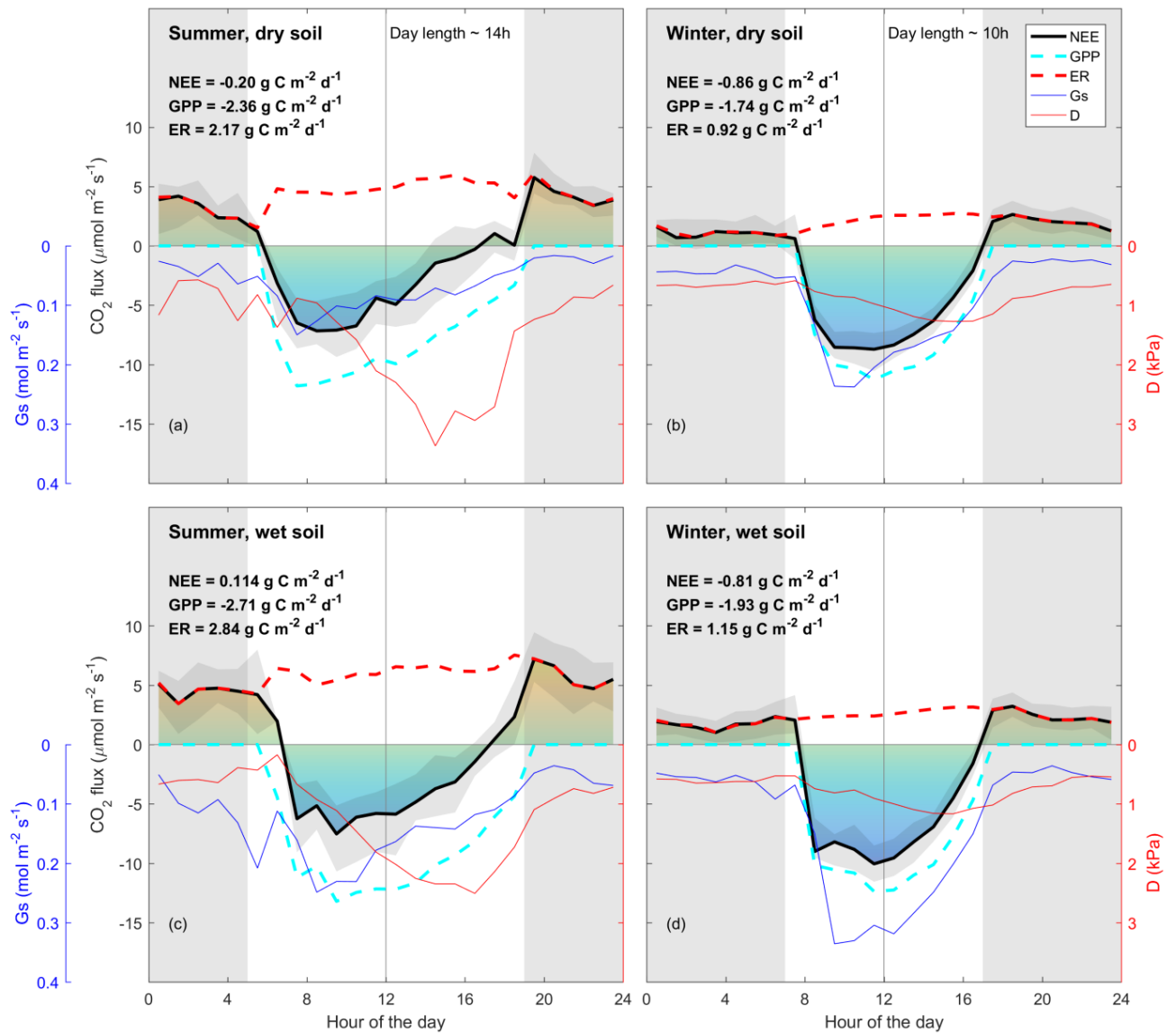
## 431 **Acknowledgements**

432 The Australian Education Investment Fund, Australian Terrestrial Ecosystem Research Network, and  
433 Hawkesbury Institute for the Environment at Western Sydney University supported this work. We  
434 thank Jason Beringer, Helen Cleugh, Ray Leuning and Eva van Gorsel for advice and support. Senani  
435 Karunaratne provided soil classification details.



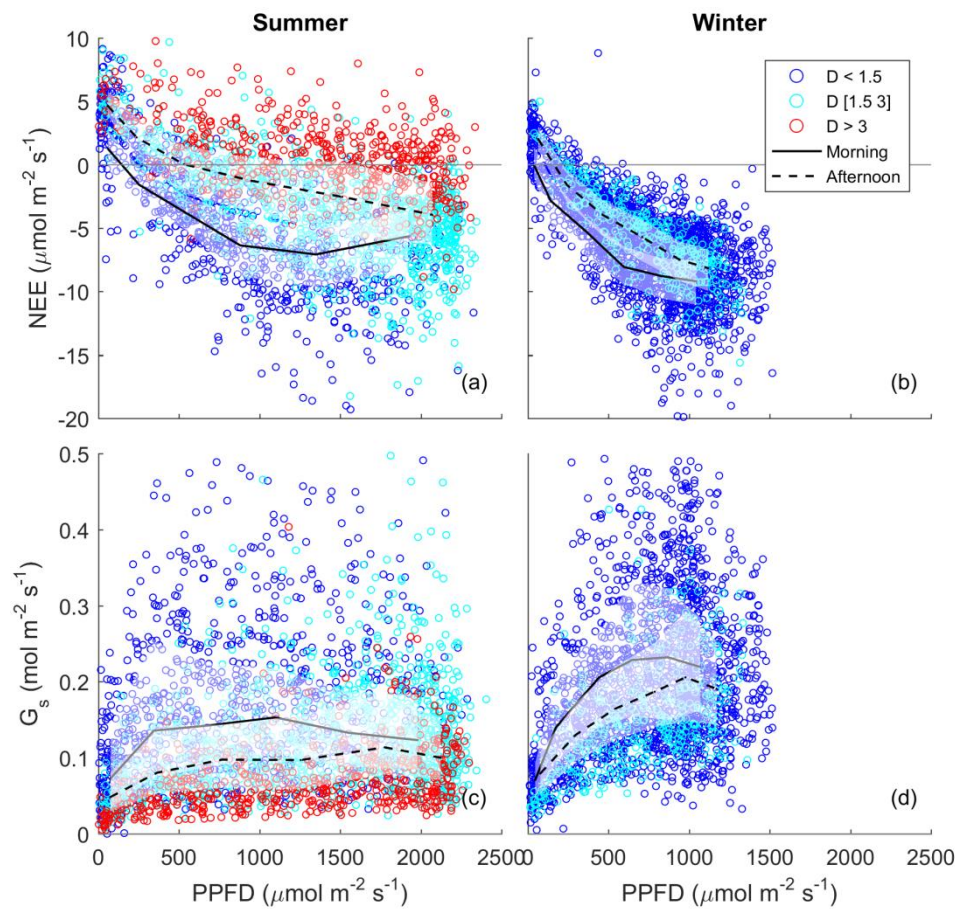
436

437 **Figure 1** a) Time series of monthly carbon flux (net ecosystem exchange (NEE), ecosystem respiration (ER) and gross  
 438 primary productivity (GPP),  $\text{g C m}^{-2} \text{ month}^{-1}$ ) (negative indicates ecosystem uptake); b) rainfall,  $\text{mm month}^{-1}$ ; soil water  
 439 content from 0 to 8 cm ( $\text{SWC}_{0-8\text{cm}}$ , %); c) average of daily maximum for each month photosynthetically active radiation  
 440 ( $\text{PPFD}_{\text{max}}$ ,  $\mu\text{mol m}^{-2} \text{ s}^{-1}$ ), air temperature ( $T_{\text{a,max}}$ ,  $^{\circ}\text{C}$ ) and vapour pressure deficit ( $D_{\text{max}}$ , kPa). d) Canopy dynamics trends:  
 441 enhanced vegetation index (EVI, unitless); leaf area index (LAI,  $\text{m}^2 \text{ m}^{-2}$ ) and litter production ( $L_p$ ,  $\text{m}^2 \text{ m}^{-2} \text{ month}^{-1}$ ). Shaded  
 442 areas shows summer (dark grey) and winter (light grey). Note  $T_{\text{a,max}}$  and  $\text{PPFD}_{\text{max}}$  remained above  $15^{\circ}\text{C}$  and  $800 \mu\text{mol m}^{-2} \text{ s}^{-1}$ .  
 443



444

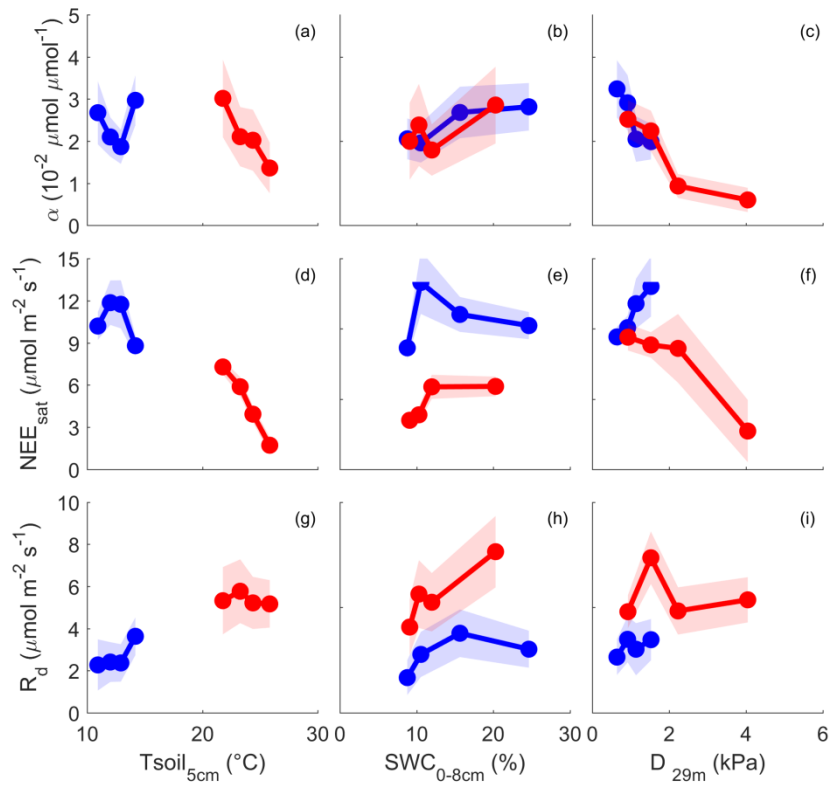
445 **Figure 2** Diurnal trend (line: median and shade: quartile) of clear-sky measured net ecosystem exchange (NEE, thick black  
 446 line,  $\mu\text{mol m}^{-2} \text{ s}^{-1}$ ); estimated daytime ecosystem respiration (ER, inferred from a neural network fitted on nighttime NEE,  
 447 thick dotted red line,  $\mu\text{mol m}^{-2} \text{ s}^{-1}$ ); estimated gross primary productivity (GPP, inferred as  $\text{NEE} - \text{ER}$ , thick dotted cyan  
 448 line,  $\mu\text{mol m}^{-2} \text{ s}^{-1}$ ); measured vapour pressure deficit (D, thin red line, kPa); and estimated surface  
 449 conductance ( $G_s$ , inferred from Penman-Monteith, blue line,  $\text{mmol m}^{-2} \text{ s}^{-1}$ ). Grey shade shows night-time (sunset to sunrise).  
 450 NEE, GPP and ER number are calculated by integrating the diurnal fluxes as shown in the figure. “Wet” and “dry” soil  
 451 is defined as below or above the median of soil water content during summer or winter. Summer is December through  
 452 February. Winter is June through August, as defined by the Sydney bureau of meteorology. Colours under NEE rate  
 453 are shown for visualisation. Note that there is an asymmetry between morning and afternoon NEE in summer, less so in winter.  
 454 Note that ecosystem respiration (nighttime NEE) is enhanced by SWC in summer, less so in winter. Data used in this figure  
 455 correspond to clear-sky half-hour values, where high quality measured data for NEE were available.



456

457 **Figure 3** Half-hourly measured NEE vs. PPFD, coloured by D (blue, D < 1.5 kPa, cyan: D [1.5-3] kPa, red: D > 3 kPa) for  
 458 (a) summer, and (b) winter periods. Raw data are binned by light levels to show median (lines) and quartiles (white shades)  
 459 for morning (continuous lines) and afternoon (dotted lines) hours separately.

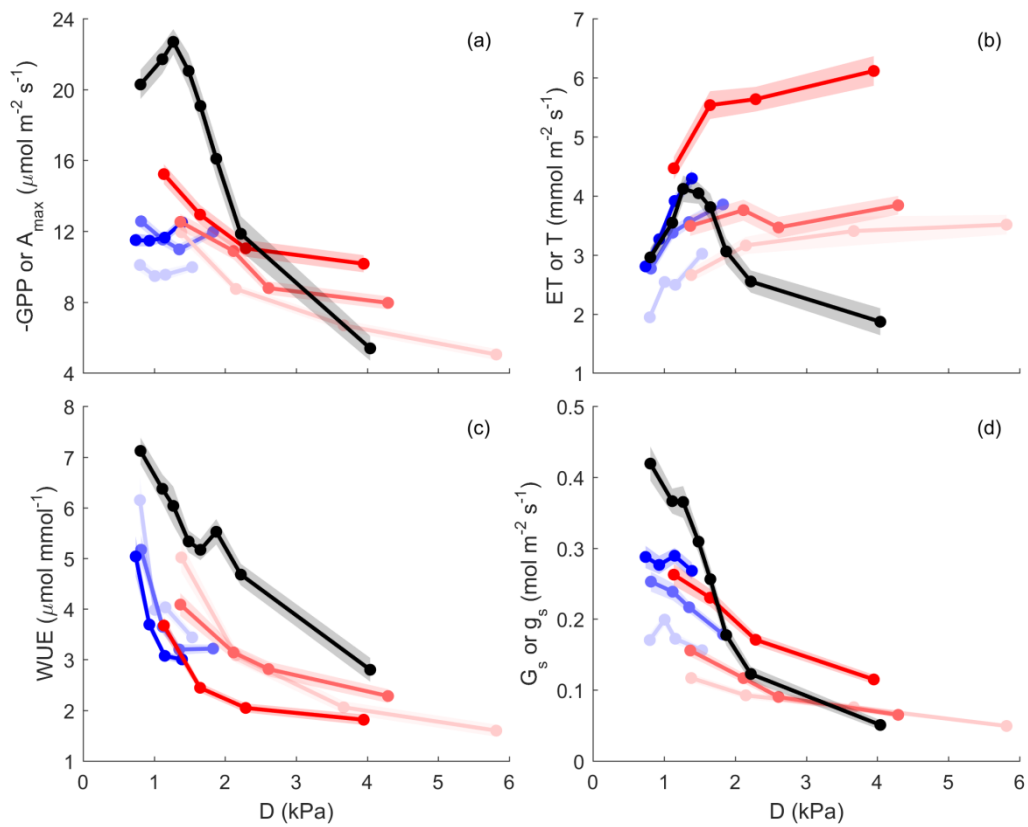




460

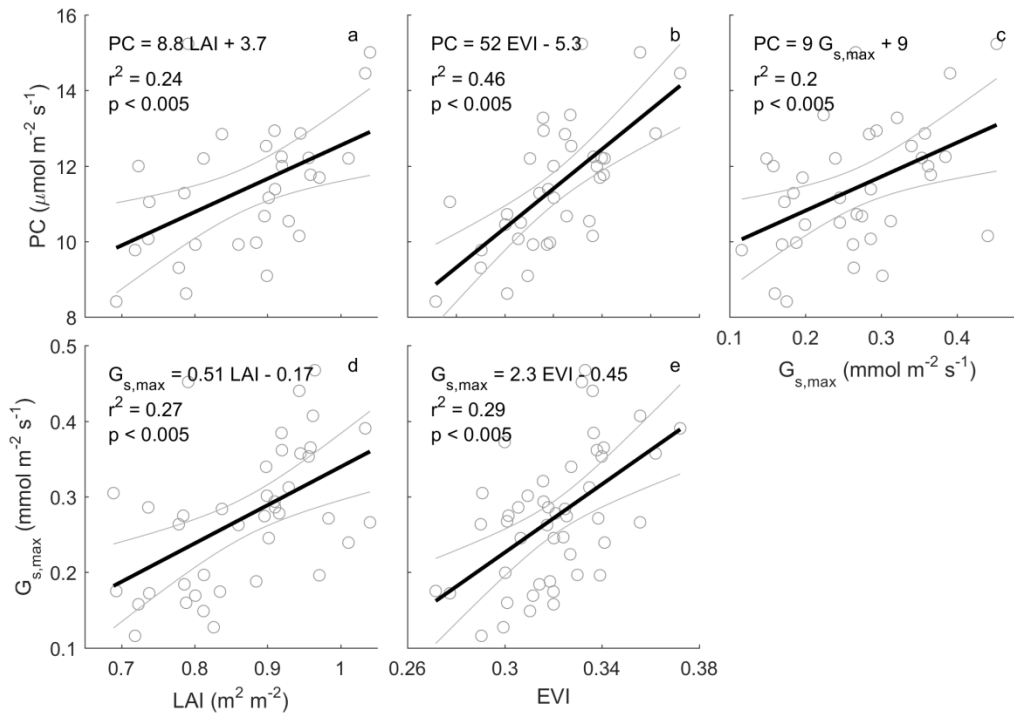
461  
462  
463  
464  
465  
466  
467

**Figure 4** NEE  $\mu\text{mol m}^{-2} \text{s}^{-1}$  light response parameters, calculated for different bins of climatic drivers (soil temperature ( $T_{\text{soil}}$ ,  $^{\circ}\text{C}$ ) at 5cm depth, soil water content (SWC, %) from 0 cm to 8 cm depth, and atmospheric demand (D, kPa) at 29 m height), only raw, qc filtered daytime data is used. Light response curve was fitted using Mitscherlich equation (see methods),  $\alpha$  is the initial slope, near PPFD = 0 ( $\mu\text{mol } \mu\text{mol}^{-1}$ ),  $\text{NEE}_{\text{sat}}$   $\mu\text{mol m}^{-2} \text{s}^{-1}$  is NEE at light saturation, and  $R_d$   $\mu\text{mol m}^{-2} \text{s}^{-1}$  is the dark respiration (NEE when PPFD = 0). Blue indicates winter months, Red indicates summer months. Dots are parameters value for each quartile of driver, plotted at  $x = \text{median}$  of driver for each bin. Shading is 95% confidence interval of the parameter fit.



468

469 **Figure 5** Gross primary productivity or net assimilation (GPP or  $A_{max}$ ,  $\mu\text{mol m}^{-2}$  [ground or leaf]  $\text{s}^{-1}$ ), evapotranspiration or  
 470 leaf transpiration (ET or T,  $\text{mmol m}^{-2}$  [ground or leaf]  $\text{s}^{-1}$ ), water use efficiency ( $\text{WUE} = \text{GPP}/\text{ET}$  or  $A_{max}/T$ ,  $\mu\text{mol mmol}^{-1}$ )  
 471 and surface conductance or leaf conductance ( $G_s$  or  $g_s$ ,  $\text{mmol m}^{-2} \text{s}^{-1}$ ) vs. vapour pressure deficit (D). Leaf level is shown in  
 472 black, ecosystem scale is shown in color; summer (red) and winter (blue), at saturated PPFD ( $>1000 \mu\text{mol m}^{-2} \text{s}^{-1}$ ). D is  
 473 binned into 4 quartiles for ecosystem and 8 for leaf; Y is mean value for each D bins, plotted at the median of D bin. Shaded  
 474 area indicates the standard error of the mean. The three color intensity show SWC quantiles (SWC  $< 0.33$ , SWC [0.33-0.67]  
 475 and SWC [0.67-1.00] shown in decreasing color intensity).



476

477  
478  
479  
480  
481  
482

**Figure 6** Relationships between monthly photosynthetic capacity (PC,  $\mu\text{mol m}^{-2} \text{s}^{-1}$ ), leaf area index (LAI,  $\text{m}^2 \text{m}^{-2}$ ),  $250 \text{ m}^2$  enhanced vegetation index (EVI), and maximum surface conductance ( $G_{s,max}$ ). Monthly PC /  $G_{s,max}$  are calculated as the median / 75% quantile of half-hourly GPP /  $G_s$  when PPFD [ $800\text{-}1200 \mu\text{mol m}^{-2} \text{s}^{-1}$ ] and D [ $1\text{-}1.5 \text{ kPa}$ ]; rain events are filtered for  $G_{s,max}$  estimation, to minimise evaporation contribution to evapotranspiration (see methods). Monthly LAI is calculated as mean of LAI smoothed by a spline. Thick black line shows a linear regression. For PC calculation, GPP data is only used when quality-checked NEE is available ( $\text{GPP} = \text{NEE measured} - \text{ER estimated by a neural network}$ , see method).

483 **Table 1** Annual precipitation (P, mm y<sup>-1</sup>), evapotranspiration (ET, mm y<sup>-1</sup>), air temperature T<sub>a</sub> (°C), net ecosystem exchange  
 484 (NEE, g C m<sup>-2</sup> y<sup>-1</sup>), gross ecosystem production (GPP, g C m<sup>-2</sup> y<sup>-1</sup>) and ecosystem respiration (ER, g C m<sup>-2</sup> y<sup>-1</sup>) for the four  
 485 year study period.

<b>Period</b>	<b>P</b> (mm y <sup>-1</sup> )	<b>ET</b> (mm y <sup>-1</sup> )	<b>T<sub>a</sub></b> (°C)	<b>NEE</b> (g C m <sup>-2</sup> y <sup>-1</sup> )	<b>GPP</b> (g C m <sup>-2</sup> y <sup>-1</sup> )	<b>ER</b> (g C m <sup>-2</sup> y <sup>-1</sup> )
<b>2014 all</b>	<b>733</b>	<b>797</b>	<b>18</b>	<b>-124</b>	<b>-1301</b>	<b>1177</b>
Winter	149	142	13	-145	-265	120
Spring	129	189	19	-20	-333	313
Summer	279	275	23	80	-302	382
Autumn	176	190	19	-39	-401	362
<b>2015 all</b>	<b>978</b>	<b>938</b>	<b>18</b>	<b>-234</b>	<b>-1517</b>	<b>1283</b>
Winter	122	160	12	-131	-335	204
Spring	237	223	19	-43	-392	349
Summer	273	318	23	24	-426	449
Autumn	345	238	18	-84	-365	280
<b>2016 all</b>	<b>893</b>	<b>852</b>	<b>19</b>	<b>-372</b>	<b>-1664</b>	<b>1292</b>
Winter	335	164	13	-130	-288	158
Spring	96	207	19	-149	-444	295
Summer	412	311	24	-8	-524	516
Autumn	50	171	20	-85	-408	323
<b>2017 all</b>	<b>821</b>	<b>798</b>	<b>19</b>	<b>-171</b>	<b>-1486</b>	<b>1315</b>
Winter	139	148	13	-177	-329	152
Spring	85	178	19	-80	-383	303
Summer	194	236	25	78	-350	428
Autumn	403	237	18	8	-424	432

486

487 **References**

- 488 Aubinet, M., T. Vesala, and D. Papale, 2012: *Eddy Covariance A Practical Guide to Measurement*  
489 *and Data Analysis*. Springer.
- 490 Aubinet, M., B. Chermanne, M. Vandenhaute, B. Longdoz, M. Yernaux, and E. Laitat, 2001: Long  
491 term carbon dioxide exchange above a mixed forest in the Belgian Ardennes. *Agricultural and Forest*  
492 *Meteorology*, **108**, 293-315.
- 493 Baldocchi, D., Y. Ryu, and T. Keenan, 2016: Terrestrial Carbon Cycle Variability. *F1000Research*, **5**.
- 494 Baldocchi, D. D., B. B. Hicks, and T. P. Meyers, 1988: MEASURING BIOSPHERE-ATMOSPHERE  
495 EXCHANGES OF BIOLOGICALLY RELATED GASES WITH MICROMETEOROLOGICAL  
496 METHODS. *Ecology*, **69**, 1331-1340.
- 497 Barr, A., and Coauthors, 2013: Use of change-point detection for friction–velocity threshold  
498 evaluation in eddy-covariance studies. *Agricultural and Forest Meteorology*, **171**, 31-45.
- 499 Beringer, J., and Coauthors, 2016: An introduction to the Australian and New Zealand flux tower  
500 network - OzFlux. *Biogeosciences*, **13**, 5895-5916.
- 501 Breiman, L., 2001: Random forests. *Machine learning*, **45**, 5-32.
- 502 Dixon, R. K., S. Brown, R. e. a. Houghton, A. Solomon, M. Trexler, and J. Wisniewski, 1994: Carbon  
503 pools and flux of global forest ecosystems. *Science(Washington)*, **263**, 185-189.
- 504 Duursma, R. A., T. E. Gimeno, M. M. Boer, K. Y. Crous, M. G. Tjoelker, and D. S. Ellsworth, 2016:  
505 Canopy leaf area of a mature evergreen Eucalyptus woodland does not respond to elevated  
506 atmospheric CO<sub>2</sub> but tracks water availability. *Global Change Biology*, **22**, 1666-1676.
- 507 Duursma, R. A., and Coauthors, 2014: The peaked response of transpiration rate to vapour pressure  
508 deficit in field conditions can be explained by the temperature optimum of photosynthesis.  
509 *Agricultural and Forest Meteorology*, **189**, 2-10.
- 510 Fan, S.-M., S. C. Wofsy, P. S. Bakwin, D. J. Jacob, and D. R. Fitzjarrald, 1990: Atmosphere-  
511 biosphere exchange of CO<sub>2</sub> and O<sub>3</sub> in the central Amazon forest.
- 512 Foken, T., 2008: The energy balance closure problem: an overview. *Ecological Applications*, **18**,  
513 1351-1367.
- 514 Foken, T., F. Wimmer, M. Mauder, C. Thomas, and C. Liebethal, 2006: Some aspects of the energy  
515 balance closure problem. *Atmospheric Chemistry and Physics*, **6**, 4395-4402.
- 516 Foken, T., M. Gockede, M. Mauder, L. Mahrt, B. Amiro, and W. Munger, 2004: Post-field data  
517 quality control. *Handbook of Micrometeorology: A Guide for Surface Flux Measurement and*  
518 *Analysis*, **29**, 181-208.
- 519 Gash, J., and A. Culf, 1996: Applying a linear detrend to eddy correlation data in realtime. *Boundary-*  
520 *Layer Meteorology*, **79**, 301-306.
- 521 Gimeno, T. E., K. Y. Crous, J. Cooke, A. P. O'Grady, A. Ósvaldsson, B. E. Medlyn, and D. S.  
522 Ellsworth, 2016: Conserved stomatal behaviour under elevated CO<sub>2</sub> and varying water availability in  
523 a mature woodland. *Functional Ecology*, **30**, 700-709.

- 524 Graham, E. A., S. S. Mulkey, K. Kitajima, N. G. Phillips, and S. J. Wright, 2003: Cloud cover limits  
525 net CO<sub>2</sub> uptake and growth of a rainforest tree during tropical rainy seasons. *Proceedings of the*  
526 *National Academy of Sciences*, **100**, 572-576.
- 527 Griebel, A., D. M. Watson, and E. Pendall, 2017: Mistletoe, friend and foe: synthesizing ecosystem  
528 implications of mistletoe infection. *Environmental Research Letters*.
- 529 Griebel, A., L. T. Bennett, D. S. Culvenor, G. J. Newnham, and S. K. Arndt, 2015: Reliability and  
530 limitations of a novel terrestrial laser scanner for daily monitoring of forest canopy dynamics. *Remote*  
531 *Sensing of Environment*, **166**, 205-213.
- 532 Hill, M. J., U. Senarath, A. Lee, M. Zeppel, J. M. Nightingale, R. D. J. Williams, and T. R. McVicar,  
533 2006: Assessment of the MODIS LAI product for Australian ecosystems. *Remote Sensing of*  
534 *Environment*, **101**, 495-518.
- 535 Hinko-Najera, N., and Coauthors, 2017: Net ecosystem carbon exchange of a dry temperate eucalypt  
536 forest. *Biogeosciences*, **14**, 3781-3800.
- 537 Hutya, L. R., and Coauthors, 2007: Seasonal controls on the exchange of carbon and water in an  
538 Amazonian rain forest. *Journal of Geophysical Research: Biogeosciences*, **112**.
- 539 Isaac, P., J. Cleverly, I. McHugh, E. van Gorsel, C. Ewenz, and J. Beringer, 2017: OzFlux Data:  
540 Network integration from collection to curation. *Biogeosciences*, **14**, 2903.
- 541 Jones, T. L., D. E. Tucker, and D. R. Ort, 1998: Chilling delays circadian pattern of sucrose phosphate  
542 synthase and nitrate reductase activity in tomato. *Plant Physiology*, **118**, 149-158.
- 543 Karan, M., and Coauthors, 2016: The Australian Supersite Network: a continental, long-term  
544 terrestrial ecosystem observatory. *Science of the Total Environment*, **568**, 1263-1274.
- 545 Keeling, C. D., S. C. Piper, R. B. Bacastow, M. Wahlen, T. P. Whorf, M. Heimann, and H. A. Meijer,  
546 2001: Exchanges of atmospheric CO<sub>2</sub> and <sup>13</sup>CO<sub>2</sub> with the terrestrial biosphere and oceans from 1978  
547 to 2000. I. Global aspects. *Scripps Institution of Oceanography*.
- 548 Keith, H., E. van Gorsel, K. L. Jacobsen, and H. A. Cleugh, 2012: Dynamics of carbon exchange in a  
549 Eucalyptus forest in response to interacting disturbance factors. *Agricultural and Forest Meteorology*,  
550 **153**, 67-81.
- 551 Knauer, J., C. Werner, and S. Zaehle, 2015: Evaluating stomatal models and their atmospheric  
552 drought response in a land surface scheme: A multibiome analysis. *Journal of Geophysical Research:*  
553 *Biogeosciences*, **120**, 1894-1911.
- 554 Knauer, J., and Coauthors, 2017: Towards physiologically meaningful water-use efficiency estimates  
555 from eddy covariance data. *Global Change Biology*.
- 556 Kolari, P., H. K. Lappalainen, H. Hänninen, and P. Hari, 2007: Relationship between temperature and  
557 the seasonal course of photosynthesis in Scots pine at northern timberline and in southern boreal zone.  
558 *Tellus B*, **59**, 542-552.
- 559 Kormann, R., and F. X. Meixner, 2001: An analytical footprint model for non-neutral stratification.  
560 *Boundary-Layer Meteorology*, **99**, 207-224.
- 561 Lim, P. O., H. J. Kim, and H. Gil Nam, 2007: Leaf senescence. *Annu. Rev. Plant Biol.*, **58**, 115-136.

- 562 Lindroth, A., L. Klemetsson, A. Grelle, P. Weslien, and O. Langvall, 2008: Measurement of net  
563 ecosystem exchange, productivity and respiration in three spruce forests in Sweden shows  
564 unexpectedly large soil carbon losses. *Biogeochemistry*, **89**, 43-60.
- 565 Lloyd, J., and J. A. Taylor, 1994: ON THE TEMPERATURE-DEPENDENCE OF SOIL  
566 RESPIRATION. *Functional Ecology*, **8**, 315-323.
- 567 Medlyn, B. E., and Coauthors, 2011: Reconciling the optimal and empirical approaches to modelling  
568 stomatal conductance. *Global Change Biology*, **17**, 2134-2144.
- 569 Mitscherlich, E. A., 1909: Das Gesetz des Minimums und das Gesetz des abnehmenden  
570 Bodenertrages. *Landw. Jahrb*, **38**, 537-552.
- 571 Moncrieff, J., R. Clement, J. Finnigan, and T. Meyers, 2004: Averaging, detrending, and filtering of  
572 eddy covariance time series. *Handbook of micrometeorology*, Springer, 7-31.
- 573 Moncrieff, J. B., and Coauthors, 1997: A system to measure surface fluxes of momentum, sensible  
574 heat, water vapour and carbon dioxide. *Journal of Hydrology*, **189**, 589-611.
- 575 Monteith, J. L., 1965: Evaporation and environment. *Symp. Soc. Exp. Biol*, **4**.
- 576 Moore, C. E., T. F. Keenan, R. A. Duursma, A. I. van Dijk, L. B. Hutley, J. R. Taylor, and M. J.  
577 Liddell, 2016: Reviews and syntheses: Australian vegetation phenology: new insights from satellite  
578 remote sensing and digital repeat photography. *Biogeosciences*, **13**, 5085.
- 579 Munné-Bosch, S., and L. Alegre, 2004: Die and let live: leaf senescence contributes to plant survival  
580 under drought stress. *Functional Plant Biology*, **31**, 203-216.
- 581 Novick, K. A., A. C. Oishi, E. J. Ward, M. B. S. Siqueira, J. Y. Juang, and P. C. Stoy, 2015: On the  
582 difference in the net ecosystem exchange of CO<sub>2</sub> between deciduous and evergreen forests in the  
583 southeastern United States. *Global Change Biology*, **21**, 827-842.
- 584 Novick, K. A., and Coauthors, 2016: The increasing importance of atmospheric demand for  
585 ecosystem water and carbon fluxes. *Nature Climate Change*, **6**, 1023-1027.
- 586 Pan, Y., and Coauthors, 2011: A large and persistent carbon sink in the world's forests. *Science*, **333**,  
587 988-993.
- 588 Pook, E., 1984: Canopy dynamics of *Eucalyptus maculata* Hook. II. Canopy leaf area balance.  
589 *Australian Journal of Botany*, **32**, 405-413.
- 590 Poulter, B., and Coauthors, 2014: Contribution of semi-arid ecosystems to interannual variability of  
591 the global carbon cycle. *Nature*, **509**, 600-603.
- 592 Prior, L. D., and D. M. Bowman, 2014: Big eucalypts grow more slowly in a warm climate: evidence  
593 of an interaction between tree size and temperature. *Global change biology*, **20**, 2793-2799.
- 594 Reich, P. B., D. S. Falster, D. S. Ellsworth, I. J. Wright, M. Westoby, J. Oleksyn, and T. D. Lee, 2009:  
595 Controls on declining carbon balance with leaf age among 10 woody species in Australian woodland:  
596 do leaves have zero daily net carbon balances when they die? *New Phytologist*, **183**, 153-166.
- 597 Resco de Dios, V., A. W. Fellows, R. H. Nolan, M. M. Boer, R. A. Bradstock, F. Domingo, and M. L.  
598 Goulden, 2015: A semi-mechanistic model for predicting the moisture content of fine litter.  
599 *Agricultural and Forest Meteorology*, **203**, 64-73.

600 Restrepo-Coupe, N., and Coauthors, 2016: MODIS vegetation products as proxies of photosynthetic  
601 potential along a gradient of meteorologically and biologically driven ecosystem productivity.  
602 *Biogeosciences*, **13**, 5587-5608.

603 Restrepo-Coupe, N., and Coauthors, 2017: Do dynamic global vegetation models capture the  
604 seasonality of carbon fluxes in the Amazon basin? A data-model intercomparison. *Global change*  
605 *biology*, **23**, 191-208.

606 Saleska, S. R., and Coauthors, 2003: Carbon in Amazon forests: unexpected seasonal fluxes and  
607 disturbance-induced losses. *Science*, **302**, 1554-1557.

608 Schimel, D. S., and Coauthors, 2001: Recent patterns and mechanisms of carbon exchange by  
609 terrestrial ecosystems. *Nature*, **414**, 169-172.

610 Thom, A., 1972: Momentum, mass and heat exchange of vegetation. *Quarterly Journal of the Royal*  
611 *Meteorological Society*, **98**, 124-134.

612 Tjoelker, M. G., J. Oleksyn, and P. B. Reich, 2001: Modelling respiration of vegetation: evidence for  
613 a general temperature-dependent Q<sub>10</sub>. *Global Change Biology*, **7**, 223-230.

614 Trenberth, K. E., 1983: What are the seasons? *Bulletin of the American Meteorological Society*, **64**,  
615 1276-1282.

616 van Gorsel, E., and Coauthors, 2013: Primary and secondary effects of climate variability on net  
617 ecosystem carbon exchange in an evergreen Eucalyptus forest. *Agricultural and Forest Meteorology*,  
618 **182-183**, 248-256.

619 Vickers, D., and L. Mahrt, 1997: Quality control and flux sampling problems for tower and aircraft  
620 data. *Journal of Atmospheric and Oceanic Technology*, **14**, 512-526.

621 Webb, E. K., G. I. Pearman, and R. Leuning, 1980: Correction of flux measurements for density  
622 effects due to heat and water vapour transfer. *Quarterly Journal of the Royal Meteorological Society*,  
623 **106**, 85-100.

624 Wilczak, J. M., S. P. Oncley, and S. A. Stage, 2001: Sonic anemometer tilt correction algorithms.  
625 *Boundary-Layer Meteorology*, **99**, 127-150.

626 Wilson, K., and Coauthors, 2002: Energy balance closure at FLUXNET sites. *Agricultural and Forest*  
627 *Meteorology*, **113**, 223-243.

628 Wilson, K. B., D. D. Baldocchi, and P. J. Hanson, 2001: Leaf age affects the seasonal pattern of  
629 photosynthetic capacity and net ecosystem exchange of carbon in a deciduous forest. *Plant Cell and*  
630 *Environment*, **24**, 571-583.

631 Windsor, D. M., 1990: Climate and moisture variability in a tropical forest: long-term records from  
632 Barro Colorado Island, Panama.

633 Wu, J., and Coauthors, 2016: Leaf development and demography explain photosynthetic seasonality  
634 in Amazon evergreen forests. *Science*, **351**, 972-976.

635 Xia, J. Y., and Coauthors, 2015: Joint control of terrestrial gross primary productivity by plant  
636 phenology and physiology. *Proceedings of the National Academy of Sciences of the United States of*  
637 *America*, **112**, 2788-2793.



- 638 Yi, C., and Coauthors, 2010: Climate control of terrestrial carbon exchange across biomes and  
639 continents. *Environmental Research Letters*, **5**, 034007.
- 640 Zhang, Y., Z. Tan, Q. Song, G. Yu, and X. Sun, 2010: Respiration controls the unexpected seasonal  
641 pattern of carbon flux in an Asian tropical rain forest. *Atmospheric Environment*, **44**, 3886-3893.
- 642